Earth Planet. Sci. Lett. 648 (2024) 119073

Contents lists available at ScienceDirect

Earth and Planetary Science Letters

journal homepage: www.elsevier.com/locate/epsl

Characterization of bedrock mass-wasting at fault-bound abyssal hills

Alex Hughes [a,b,*], Jean-Arthur Olive [c], Luca C. Malatesta [d], Javier Escartín [c]

[a] Institut de Physique du Globe de Paris, CNRS, Université de Paris, Paris F-75005, France
[b] Department of Earth, Ocean, and Atmospheric Sciences, University of British Columbia, Vancouver, BC, Canada
[c] Laboratoire de Géologie, Ecole Normale Supérieure - CNRS - PSL University, Paris, France
[d] Earth Surface Process Modelling, GFZ German Research Center for Geosciences, Potsdam, Germany

ARTICLE INFO

Edited by: J.P. Avouac

ABSTRACT

Fault-bound abyssal hills form at mid-ocean ridges and cover ~65 % of Earth's surface, but few studies have characterized the extent to which bedrock erosion controls their morphology. Here, we use bathymetry data to characterize the morphology of fault-bound abyssal hills on a global scale, and employ numerical modelling and seismicity catalogues to quantify how simultaneous rock uplift and bedrock erosion sculpt deep-ocean landscapes. By generating a global database on abyssal hill morphology, we show that most large abyssal-hill scarps (>100 m in height) within the near-axis zone of seismicity (i.e., <30 km from axis) have slopes between 10 and 30°, well below the expected range of underlying normal fault dips of 45–60°. We interpret this as a manifestation of efficient bedrock mass wasting on near-axis growing faults, a process that operates from fault inception. Using a non-linear topographic diffusion model to parameterise the effects of erosion, we find a balance between erosion and rock uplift that is similar for slow, intermediate, and fast spreading rates. We express the ratio of erosion to uplift as an inverse Peclet number that ranges between 0.06 and 0.82 for abyssal hills. We also calculate a global bedrock diffusivity for abyssal hills in the range 0.01–1.51 $m^2\ yr^{-1}$. These results imply that bedrock erosion is a significant process that sculpts abyssal hill morphology and reshapes the oceanic crust. Overall, this study provides a framework to incorporate bedrock mass wasting into future models of ocean-floor evolution and, more generally, to active extensional settings on Earth and beyond.

1. Introduction

Abyssal hills cover approximately 65 % of the Earth's seafloor. These elongated, regularly-spaced topographic highs form at mid-ocean ridges (MORs, Fig. 1a) where normal faults uplift and tilt freshly-accreted basaltic seafloor (e.g., Macdonald et al. 1996). While the mechanisms responsible for fault formation and tectonic uplift at MORs are reasonably well understood (Goff, 1991; Buck et al., 2005; Olive et al., 2015), relatively little is known about the erosive processes sculpting these submarine landscapes. It is often assumed that erosion only has a second-order impact on the morphology of uplifting abyssal hills, and that bathymetry faithfully records tectono-magmatic processes (e.g., Cowie et al. 1993, Bohnenstiehl and Carbotte 2001, Paulatto et al. 2015, Goff 2020). This assumption is challenged by high-resolution seafloor surveys that reveal widespread rockslides on the active fault scarps that delineate MOR axes (Allerton et al., 1995; Goff and Tucholke, 1997; Searle et al., 1998; Mitchell et al., 2000; Cannat et al., 2013). However, these high-resolution studies are conducted primarily at local scales, near MOR axes, and we lack a global assessment of bedrock mass wasting. Researchers have previously attempted to quantify erosion and transport of pelagic sediments on the abyssal plain (Webb and Jordan, 1993; 2001; Mitchell, 1995; 1996). More recent endeavors have started to quantify active bedrock erosion on the ocean-floor more generally (Hilley et al., 2020; Hughes et al., 2021; 2023). Despite these efforts, a quantitative framework to describe the evolution of tectonically-active bedrock landscapes at the scale of the ocean floor has proven difficult to establish because the distribution, frequency, and magnitude of gravitational mass wasting remain largely unknown.

On land, landslides are recognized as key drivers of landscape evolution (e.g., Densmore et al. 1997, Roering et al. 1999). The difficulty in subaerial studies lies in teasing out the influence of rainfall, soil strength, topographic stresses, vegetation cover, and seismic activity on the time-averaged erosion rates that result from repeated landslides (e.g., Rodríguez et al. 1999, Malamud et al. 2004, Hovius et al. 2011). Farther afield on the icy moons of Jupiter and Saturn, recent work identified ground accelerations from moonquakes as the principal driver

* Corresponding author at: Department of Earth, Ocean, and Atmospheric Sciences, University of British Columbia, Vancouver, BC, Canada.
E-mail address: dralexhughes84@gmail.com (A. Hughes).

https://doi.org/10.1016/j.epsl.2024.119073
Received 18 June 2024; Received in revised form 2 October 2024; Accepted 12 October 2024
Available online 28 October 2024

of mass wasting along tectonics ridges (Mills et al., 2023). Back on Earth, fault scarps and fault-bound abyssal hills that formed along MORs (herein collectively referred to as abyssal hills) experience no precipitation-driven or vegetation-modulated erosion processes. The absence of these key variables, combined with rapid seismogenic uplift of lithologically-uniform basaltic bedrock make abyssal hills an ideal endmember setting to explore how mass wasting shapes topography on Earth and beyond.

Earthquakes can be important drivers of submarine erosion (Hughes et al., 2021; 2023). Observations from bathymetry, side-scan sonar, and seismicity data show that abyssal hill faults grow within a 2 to 30 km wide window from the ridge axis (Alexander and Macdonald, 1996; McAllister and Cann, 1996; Searle et al., 1998; Bohnenstiehl and Carbotte, 2001; Smith et al., 2003). In areas with pronounced ridge shoulders, abyssal hills may even experience a reduction in amplitude between ~10 and ~30 km off-axis, due to reverse slip along hill-bounding faults associated with reverse earthquakes (Deffeyes, 1970; Olive et al., 2024). The presence of thin fingers of fresh bedrock talus at the base of growing abyssal hills has been taken to indicate active faulting under the assumption that mass wasting is mostly triggered by earthquakes (Fig. 2a; Searle et al., 1998; Escartín et al., 1999). As fault throw evolves, mass wasting erodes the fault scarp and buries its base before eventual blanketing by pelagic sedimentation (Fig. 2a–b; Allerton et al., 1995; Goff and Tucholke, 1997). Prior studies have used seafloor slopes to calculate diffusivity values that describe the redistribution of pelagic sediments away from the ridge axis at rates of 0.007–10 m^2yr^{-1} (Webb and Jordan, 1993; 2001; Mitchell, 1995; 1996). However, without information on the spatial and temporal evolution of abyssal hill bedrock erosion, we have insufficient data to assess the impact of mass wasting on the morphology of growing abyssal hills. Ultimately, such estimates are required to use bathymetry as a reliable recorder of tectonic and magmatic processes at MORs (Cowie et al., 1993; Bohnenstiehl and Carbotte, 2001; Paulatto et al., 2015).

Abyssal hill morphology varies with spreading rate and embeds, to first order, the modulation of fault activity by MOR magmatism (Fig. 1c; Goff, 1991; Buck et al., 2005; Roth et al., 2019; Tucholke et al., 2023). At fast-spreading ridges (>75 mm yr^{-1} full spreading rate), magmatic emplacement in the brittle lithosphere accounts for greater plate separation than at slow spreading ridges (<55 mm yr^{-1}). Faults at fast ridges rapidly migrate off-axis where they are abandoned (Buck et al., 2005; Behn and Ito, 2008; Olive et al., 2015). As a result, abyssal hills at fast ridges have less relief (≤100 m) and are more closely spaced than those at slow ridges, where they grow taller (~1000 m) and, eventually, more widely-spaced (e.g., Goff 1991, Goff et al. 1997, Roth et al. 2019, Goff 2020). As a corollary, faults at fast and slow spreading ridges could potentially slip at similar rates (e.g., a slip rate that is 10 % of a fast spreading rate like 10 cm/yr is the same as 50 % of a slow rate like 2 cm/yr). The seismogenic behavior of MOR faults also appears modulated by spreading rate, with a lesser seismic moment release rate measured at faster ridges (Cowie et al., 1993; Frohlich and Wetzel, 2007;

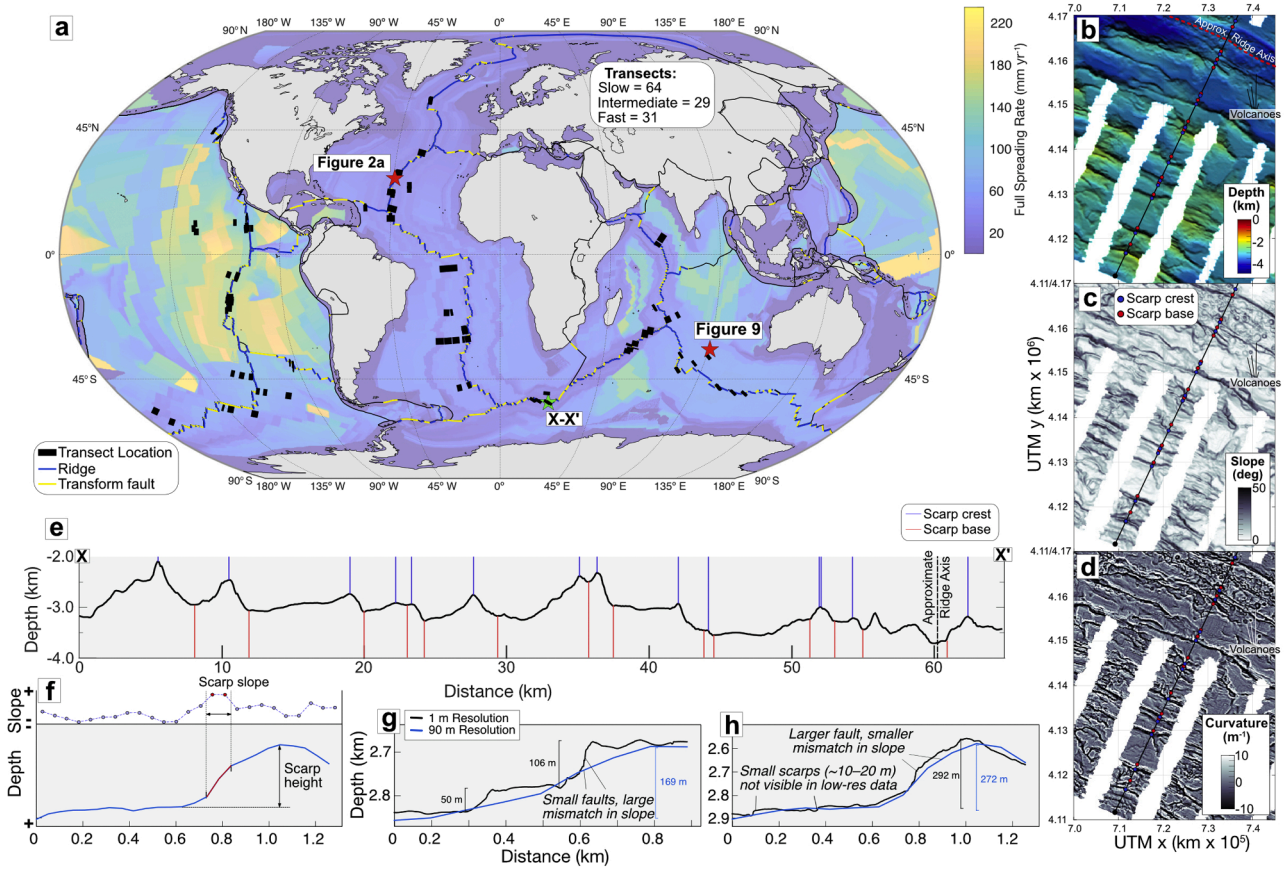

Fig. 1. Summary of datasets and methods. (a) Global spreading rate map (Seton et al., 2020) and location of the transects measured in this study. Plate boundaries are from Bird (2003). The green star locates example profile in Fig. 1e. Thin black lines are non-ridge plate boundaries. (b) Shaded relief bathymetry, (c) slope, and (d) curvature maps used to identify faults at the Southwest Indian Ridge. UTM = Universal Transverse Mercator. Maps in UTM zone 34S. (e) Example profile along black line in parts b-d showing picks for fault scarp crests (blue lines) and bases (red lines) used to constrain scarp height. (f) Schematic diagram showing how we measured height and slope. Upper: slope profile (blue dots); lower: bathymetry (blue line). Here, slope is the average from a slope profile section (from the red dots) along the steepest scarp section (red line). (g) Comparison of scarp morphology between shipboard bathymetry (90 m resolution) and near-bottom bathymetry (1 m resolution) showing the potential underestimation of slope by shipboard data. (h) Comparison of scarp morphology between shipboard bathymetry and near-bottom bathymetry data showing general agreement of slopes for scarps >200 m height. See Fig. S1 for line and location of profiles in parts f–h.

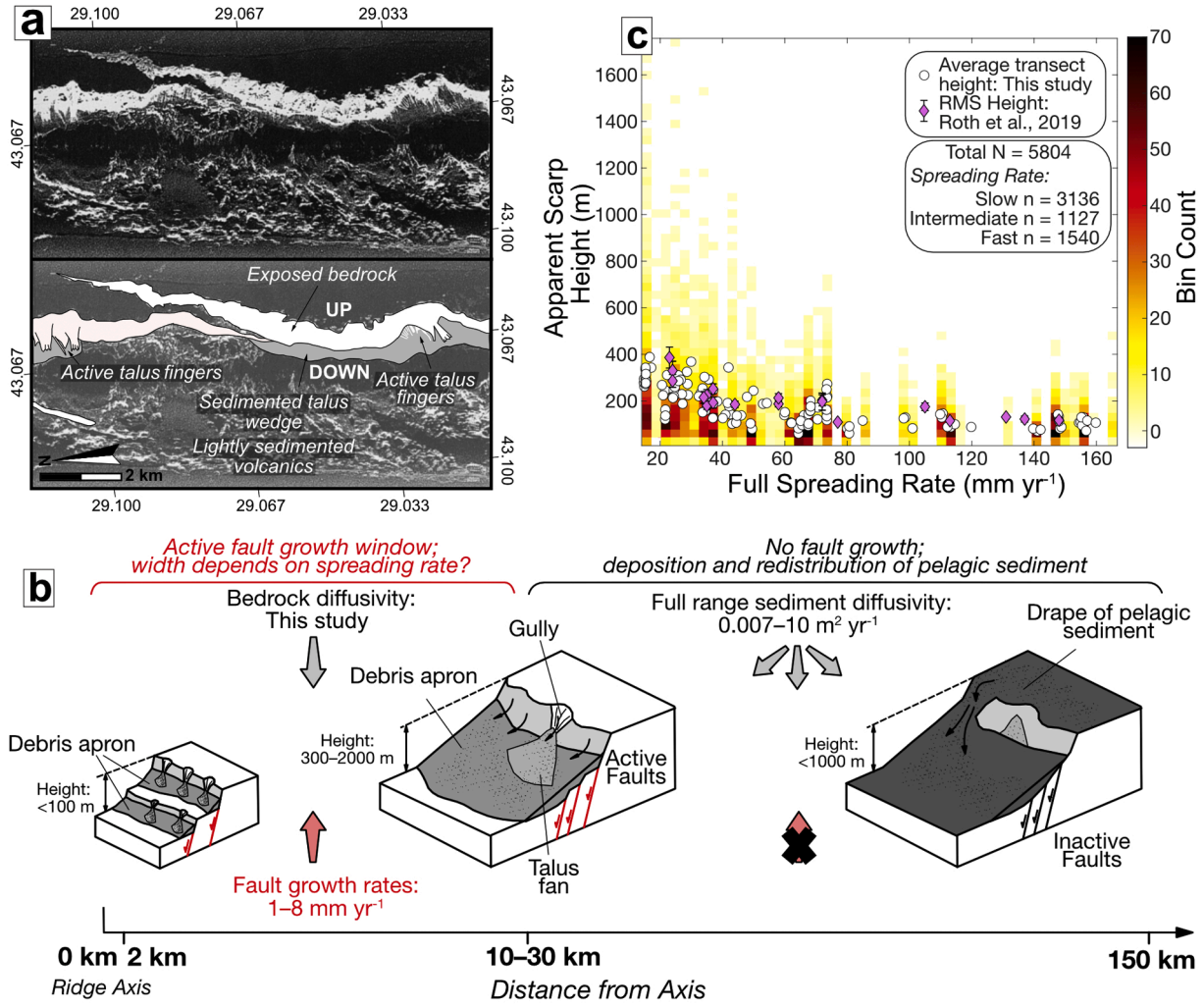

Fig. 2. (a) Deep-towed sonar image from Searle et al. (1998) showing recent active bedrock mass wasting at 29° N on the Mid-Atlantic ridge. Strong acoustic backscatter is white and indicates bedrock or bedrock talus while weak acoustic reflections are dark gray and represent sediment cover. Black areas are acoustic shadows. In the interpretation sketch, bedrock or fresh bedrock talus on the scarp face is highlighted in white and sediment in grey. Location is shown in Fig. 1a. (b) Schematic diagram showing scarp evolution with increasing distance from the ridge axis after Allerton et al. (1995). Rates for sediment diffusivity are from Webb and Jordan (2001). Range of fault growth rates are from McAllister and Cann (1996) and Cowie et al. (1993). (c) Density plot of height as a function of spreading rate for scarps analyzed here. Density is the number of hills within each bin of width ~3.33 mm yr^{-1} and height ~35 m. Average values for each transect (white circles) are for comparison with the root-mean squared heights of abyssal hills from Roth et al. (2019) (purple diamonds).

Mark et al., 2018). To untangle the respective roles that the total duration of fault slip and the associated seismic moment release play in shaping abyssal hill morphology through gravitational mass wasting, we assembled an extensive dataset of fault scarp parameters, across a wide range of MOR spreading rates. We focused on the entire erosional history of abyssal hills starting at the ridge axis (Figs. 1a, 2c) and measured the height and slope of global abyssal hill scarps to characterize spatiotemporal variations in morphology. We then used our global database to constrain a numerical model for abyssal hill erosion using non-linear topographic diffusion laws, which are commonly applied to subaerial hillslopes (e.g., Roering et al. 1999) and to the redistribution of pelagic sediment on abyssal hills (e.g., Webb and Jordan 2001). Outputs from the models were used to evaluate the ratio of rock uplift to erosion for abyssal hills globally.

2. Geomorphic analysis

2.1. Quantification of scarp morphology

We compiled scarp parameters from abyssal hills within 2500 km of the global mid-ocean ridge system to sample a broad range of erosional and tectonic histories across all spreading rates. We focused on areas with well-lineated abyssal terrain, and avoided transects across transform valleys. We also avoided complex tectonic areas such as those with prominent detachment faulting linked to reduced melt supply (e.g., Escartín et al. 2008, Smith et al. 2014) or non-transform offsets. We extracted 124 spreading-parallel transects (Fig. 1a) in areas with high-resolution, publicly available, shipboard multibeam bathymetry data (Global Multi-Resolution Topography Data Synthesis: https://www.gmrt.org/index.php; Ryan et al., 2009). The transect length (horizontal distance between first and last scarp crests), is limited by bathymetric data availability at each location and ranges from 45 to 490 km. We measured scarp morphology from digital elevation models (Fig. 1b–f) and resampled all data at the highest common resolution of 100 m to avoid resolution-dependent slope artifacts.

We measured the height, slope, and distance to the ridge axis for 5803 abyssal hill faults from the 124 transects following the method of Howell et al. (2016) illustrated in Fig. 1, and described in the Supplementary Materials. We also recorded the crustal age and spreading rate for each fault, based on global grids of age and spreading rate (Seton

et al., 2020). For our analysis, we binned the data based on spreading rate as slow (<55 mm yr^{-1}), intermediate (55–75 mm yr^{-1}), and fast (≥75 mm yr^{-1}), with 3136, 1127, and 1540 hills in each bin, respectively. We combined ultra-slow with slow ridges and ultra-fast with fast ridges (e.g., Dick et al. 2003) to maximize the data in each bin.

2.2. Slope measurements in shipboard bathymetry

Due to the limited resolution of shipboard multibeam bathymetry in the deep ocean (typically 50–100 m resolution), small scarps (<100 m height) are best analyzed using near-bottom bathymetry data acquired with underwater vehicles at horizontal resolutions of a few meters (Le Saout et al., 2018; Hughes et al., 2021). However, these datasets are scarce at MORs and focus primarily on the axial area (Cannat et al., 2013; Smith et al., 2014; Le Saout et al., 2018). Studies of tall abyssal hill scarps (>100 m) at meter-scale resolution are restricted to very few sites (Cannat et al., 2013). Therefore, variations in abyssal hill morphology can only be studied globally using shipboard multibeam bathymetry (Fig. 1).

For small faults from 2D shipboard bathymetric profiles, slope can be underestimated due to the data resolution (Fig. 1g). Bathymetry gridded with a resolution of 100 m $pixel^{-1}$ cannot resolve slopes >45° for scarps shorter than 100 m. Even for scarps >100 m tall, shipboard bathymetry can underestimate the true local slope for stepped scarps on a scale not resolvable at that resolution (e.g., several adjacent faults; Fig. 1g). When scarps grow taller than ~100–200 m, the slope measured from shipboard bathymetry approaches that measured in near-bottom, high-resolution bathymetry (Fig. 1h). To minimize spurious slopes due to data resolution (see 4.1), we focused our analysis on faults >100 m in height (3516 out of 5804 faults) and on time-averaged mass wasting (as opposed to individual rocksliding events) on the largest abyssal hills. The full database of global abyssal hill morphology is included in the supplementary materials.

2.3. Trends in abyssal hill morphology

From the database, we documented an overall decrease in scarp height with increasing spreading rate, consistent with independent studies (Figs. 2c, 3a; e.g., Goff 1991, Goff et al. 1997, Roth et al. 2019, Goff 2020). This agreement confirms that our scarp picks constitute a representative abyssal hill population. Crucially, almost all measured slopes (3506 out of 3516) are below the 45–60° range of fault dips suggested for mid-ocean ridge faults (Fig. 3b; Thatcher and Hill, 1995).

To characterize scarp height and slope evolution with increasing age and distance from the ridge axis (Figs. 2b, 3c–f, S5–S7), we used the 95th percentile. Because the data show significant and expected scatter, trends in the median value are subdued and the 95th percentile best records key overall trends in fault morphological evolution. There is a rapid increase in the height and slope of the largest scarps within 10 km of the ridge axis, with maximum values of 1750 m and 55° by ~7 km and ~6 km from the axis, respectively (Figs. 3c–d, 4b–c). The 95th percentiles of height and slope decrease rapidly from a peak of 700 m and 37° at 5–10 km from the axis, before levelling off between 300 and 400 m and 20–25° at distances beyond 500 km (Fig. 3c–d). The abrupt end to scarp height increase at ~10 km off-axis is consistent with the unfaulting process described by Olive et al. (2024). Farther off-axis over increasingly old seafloor, there is a subtle but gradual decrease in the 95th percentile of scarp height from 700 m at 20 Ma and 37° at 5 Ma down to ~500 m at ~60 Ma and ~30° at 40 Ma (Fig. 3e). This slow decay, over hundreds of km, is likely related to pelagic sedimentation filling topographic lows. In fact, typical sedimentation rates are consistent with the observed rate of apparent relief reduction in old seafloor (Fig. 3e). Plots of morphological data for slow, intermediate, and fast spreading rates are included in the supplementary materials (Figs. S5–S7).

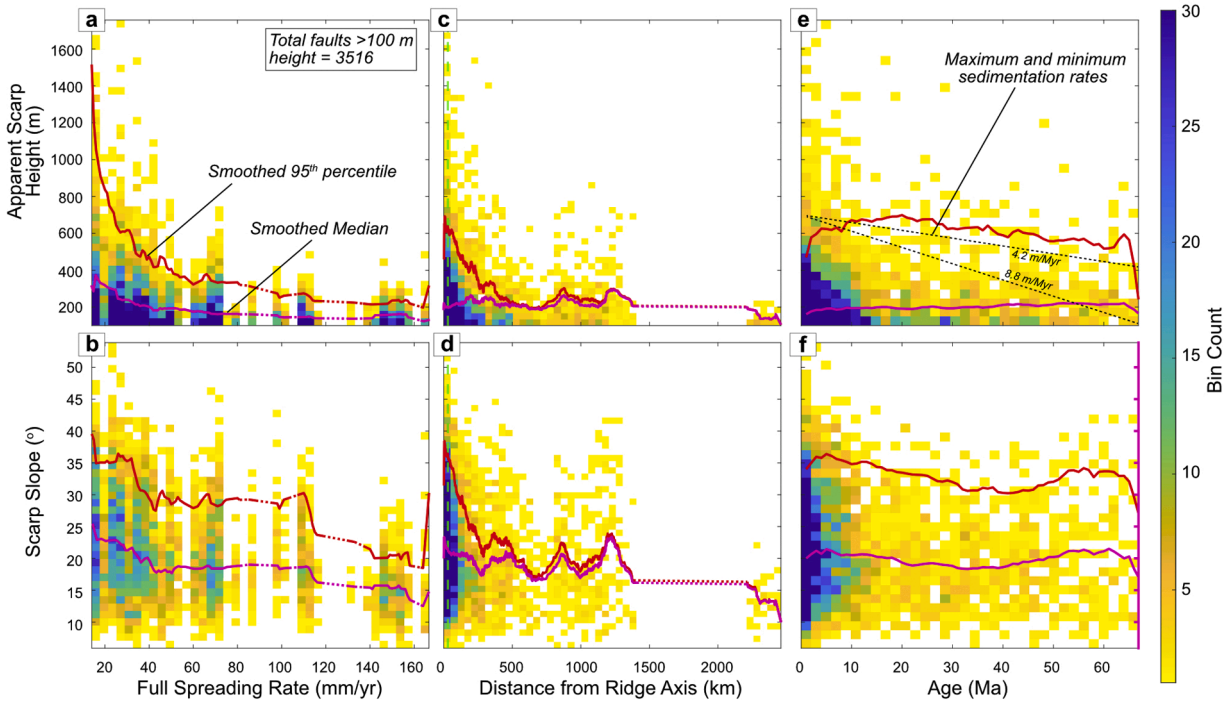

Fig. 3. Density plots showing the morphological data for abyssal hills >100 m in height. Red lines are smoothed 95th percentiles and the dashed lines are areas with no data. (a–b) Height and slope as a function of increasing full spreading rate. The bin width for spreading rate is ~3.3 mm/yr, height is binned in ~41 m increments, and slope in ~1.3° increments. The 95th percentile is smoothed using a window of +/ 5 mm/yr. (c–d) Height and slope as a function of distance from the ridge axis. The bin width for distance is ~50 km, height is binned in ~36 m increments, and slope in ~1.0° increments. The 95th percentile is smoothed using a window of +/ 25 km. (e-f) Height and slope as a function of age. The bin width for age is 2 Ma, height is binned in ~52 m increments, and slope in ~1.6° increments. The 95th percentile is smoothed using a window of +/ 10 Ma. The sedimentation rate in (e) shows the reduction in fault scarp height (initially 700 m), assuming infill of adjacent topographic lows. Sedimentation rates are based on a value of 6.5 +/- 2.3 m/Myr (Webb and Jordan, 2001).

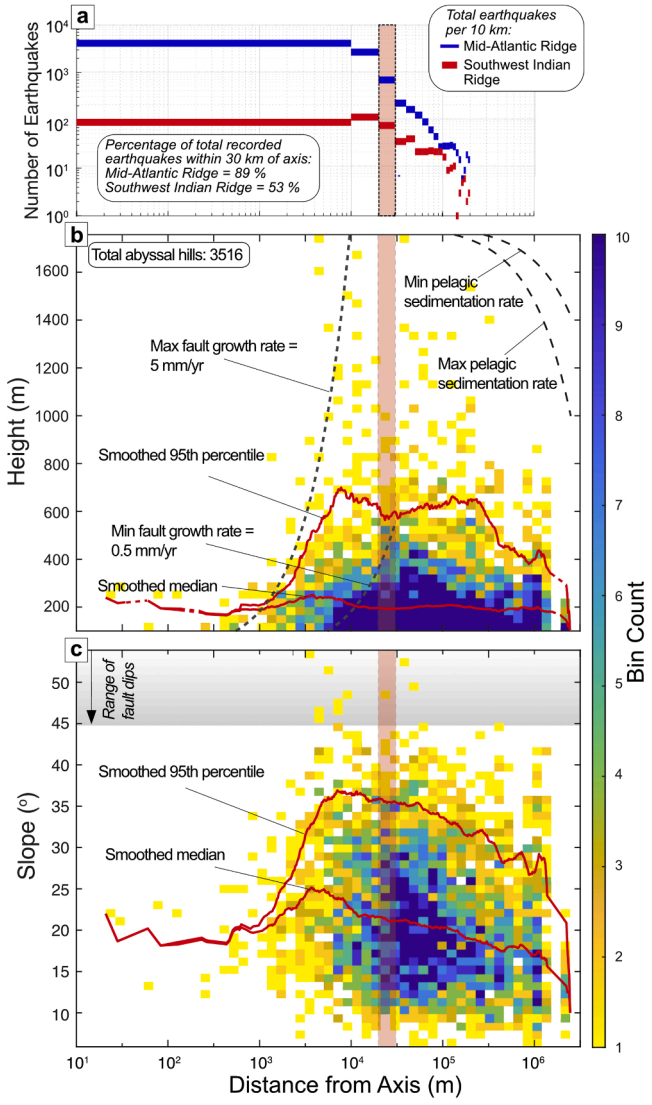

Fig. 4. (a) Decreasing earthquake frequency with increasing distance from the ridge axis in 10 km bins recorded with a hydrophone array from the Mid-Atlantic ridge for the period 1999–2003 (Bohnenstiehl and Carbotte, 2001; Smith et al., 2003) and the Southwest Indian Ridge for the period 2012–2013 (Tsang-Hin-Sun et al., 2016). Both datasets have a magnitude range between ~205 and 245 dB (~M_w 2.5–6.5) and include some transform seismicity. (b) Density plot for abyssal hills >100 m in height showing a rapid increase in scarp height within 10 km of the ridge axis for the largest scarps defined by the 95th percentile. Sedimentation rates are based on 6.5 +/- 2.3 m/Myr (Webb and Jordan, 2001). (c) Density plot showing evolution of slope with distance to the ridge axis for abyssal hills > 100 m in height. Measured slopes are well below the assumed minimum fault dip of 45° for all but 10 data points and the moving median value of slope is generally 20–30°. The red box denotes the 20–30 km outer edge of the fault growth window. The median and 95th percentiles (red lines) in parts b and c were smoothed using a moving average filter with a smoothing window of 50 km.

2.4. Erosion during scarp growth

The geomorphological data documents the simultaneous growth and erosion of abyssal hills by fault slip and bedrock mass wasting. Abyssal hills grow within at least 10 km of the ridge axis, and possibly as far as 30 km (Fig. 4b, Table S1; Alexander and Macdonald, 1996; McAllister and Cann, 1996; Searle et al., 1998; Bohnenstiehl and Carbotte, 2001; Smith et al., 2003). We herein refer to the area of abyssal-hill growth within ~30 km of the ridge axis as the "fault growth window", but fault activity within the ridge shoulder may combine reverse and normal slip (Deffeyes, 1970; Olive et al. 2024). In this window, many abyssal hills exhibit slopes below 30° and almost all abyssal hills >100 m in height have slopes well below the assumed dip of underlying faults (45–60°; Fig. 4c; Thatcher and Hill, 1995). We suggest this discrepancy indicates erosion via bedrock mass wasting during scarp growth. Slope degradation results from the combined removal of material from the scarp face and talus deposition at its base (Fig. 2). In some cases, small, closely spaced scarps may be identified as a single unit in lower resolution data (Fig. 2g). Removing scarps <100 m in height partially mitigates their inclusion in our analysis.

The evolution of scarp slope as a function of scarp height thus captures the early tectonically driven scarp growth and decay with the increasing importance of mass wasting as a control on scarp morphology (Fig. 5). We analyzed the smoothed median of abyssal hills within the fault growth window assuming that the upper and lower limits of the data envelope record minimum and maximum amounts of scarp degradation, respectively (Fig. 5a). Overall, the smoothed median of slope for abyssal hills increases non-linearly with height (Fig. 5a). The upper envelope of slope vs. scarp-height (upper black dashed line in Fig. 5a) reaches a maximum value of ~55° for ~300 m high hills before gradually decreasing to ~45° for the tallest hills. Conversely, the lower envelope increases gradually to a maximum slope of ~40° for the tallest scarps (~1750 m high, Fig. 5a). A boundary for the theoretical maximum slope resolvable at a given horizontal resolution can be obtained using arctan(height/resolution) (black long-dashed line in Fig. 5a for a horizontal resolution of 100 m). Notably, the upper envelope lies beneath the resolution envelope for scarps below ~300 m in height. This data gap could suggest efficient erosion lowering the scarp slope away from the fault plane dip angle during growth. Alternatively, this gap could be an artifact of the coarse resolution of the data.

The evolution of slope against height can be framed as a hysteresis loop. The raising limb is defined by younger abyssal hills (<20 Ma), which have median slopes 3–5° higher than abyssal hills >20 Ma (Fig. 5b). Abyssal hills >20 Ma define the falling limb where the 95th percentile of slope for a given height is between 5 and 10° lower than abyssal hills <20 Ma (Fig. 5b). We interpret lowered slopes for older abyssal hills to represent the gentle smoothing of bathymetry by pelagic sediment deposition and redistribution (Fig. 2b; e.g., Webb and Jordan, 2001; Tominaga et al., 2011).

3. Quantifying oceanic basement erosion

We designed a numerical model to approximate how mass wasting reworks abyssal hills and infer global rates of seafloor bedrock mass wasting from the abyssal hill dataset.

3.1. Scarp evolution as a diffusive process

We simulated 1-D (across-strike) scarp morphology based on realistic erosion parameters for comparison with the quantitative data from abyssal hills presented in Section 2. At the 100 m resolution used here, one cell may encompass a wide range of erosional and depositional processes. The bathymetric data therefore reflects scarp evolution with mass transfer from steep erosive to gentle depositional sections of the scarp. We chose to parameterize mass wasting as a non-linear diffusive process, with local downslope mass flux increasing non-linearly with local topographic gradient and increasing rapidly for slopes beyond a critical failure angle (θ_c). This framework is commonly applied to model subaerial hillslopes (e.g., Roering et al. 1999), and similar diffusion equations have been used to study redistribution of pelagic sediment on abyssal hills (Webb and Jordan, 1993; 2001; Mitchell, 1995; 1996; Tominaga et al., 2011). To convey the efficiency of scarp diffusion as a competition between erosion and rock uplift, we non-dimensionalized our model inputs as an inverse Peclet number (Pe^{-1}). Pe^{-1} is the ratio of diffusion (K) relative to advection (in this case fault throw rate) and is

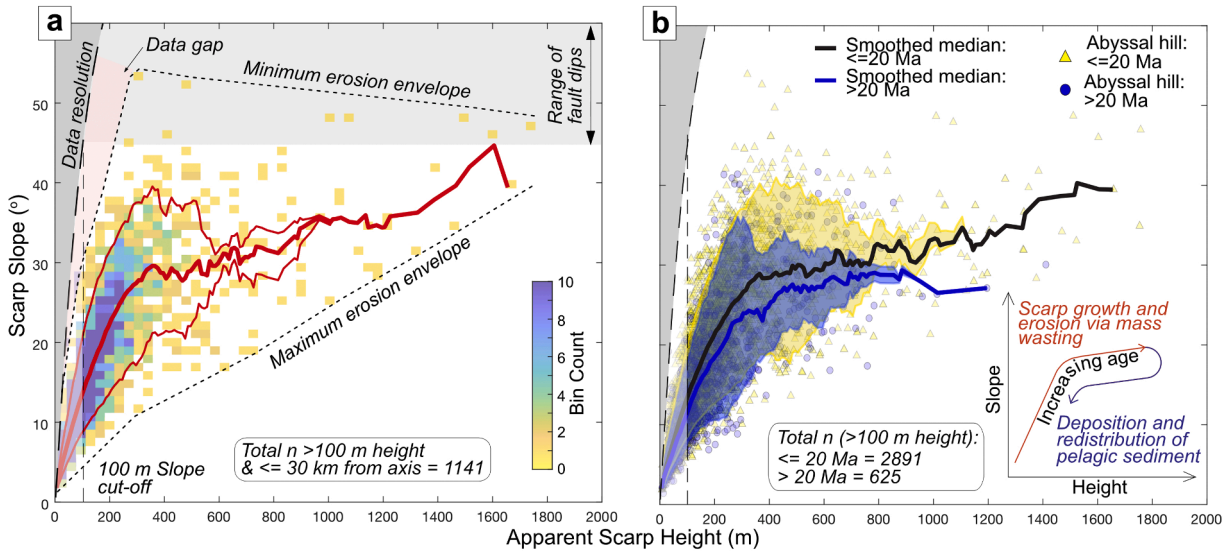

Fig. 5. (a) Density plot of slope as a function of height for global abyssal hills taller than 100 m and within 30 km of ridge axis overlain with interpretation. Maximum and minimum erosion envelopes are hand drawn. The thick red line is the smoothed moving median from 10 m bins of height and the thinner red lines are the 5th and 95th percentiles. (b) Comparison of height and slope for abyssal hills younger and older than 20 Ma. The >20 Ma bracket includes hills up to 67 Ma. The yellow (<= 20 Ma) and blue (> 20 Ma) shaded areas show the range of the data for each age bracket defined by the 5th (lower) and 95th (upper) percentiles. The inset shows schematically how abyssal hill morphology evolves similar to a hysteresis loop due to a temporal evolution in erosional and depositional process.

reflected in the evolution of abyssal hill slope with increasing height (Fig. 5a). This approach also allowed us to quantify K for a given rate of rock uplift at abyssal hills.

Our simplified approach includes a number of assumptions. We assumed that *in situ* bedrock is pervasively fractured as often observed in submersible dives from axial valley floors (e.g., Wright et al. 1995). We accounted for variation in the degree of disaggregation by running models using a critical angle of 35° and 40° (Table S2). The model also does not account for other processes that control effective strength, like cohesion or compressive strength. Additionally, sediment transport distance is a product of momentum as well as slope (Fig. 5), but the model does not incorporate varying transport distance resulting from different failure methods (e.g., rockfall, debris flow etc.). In the model, deposited volume roughly equals sediment flux (volume conservation), so we assume that porosity and, therefore, volume of intact but pervasively fractured bedrock is similar to that of bedrock talus. The non-uniform distribution of talus on hills of similar heights and at similar distance from the ridge axis (Allerton et al., 1995) suggests some spatial variability in effective rock strength and, therefore, critical failure angle. Conversely, the relatively flat geometry of the median slope for a given height in abyssal hills >20 Ma supports a threshold behavior inherent in our non-linear diffusion model. Nevertheless, our approach provides a first-order approximation of the time-averaged effect of bedrock mass wasting along abyssal hills. Alternative methods, like advection based on progressive rather than critical failure, or a lattice grain model for hillslope evolution (Tucker et al., 2018), may also be appropriate but were not considered further.

3.2. Model setup

In the model, 1-D seafloor topography along a spreading-parallel direction, $h(x,t)$, follows the following equation:

$$\frac{Dh}{Dt} = \frac{\partial}{\partial x}\left(K(\theta)\frac{\partial h}{\partial x}\right), \tag{1}$$

where $\frac{Dh}{Dt}$ denotes the Lagrangian derivative of topography as it is advected both horizontally and vertically by a steady tectonic velocity field ($v_x(x)$, $v_z(x)$). We only considered relief growth on the footwall side, i.e., $x \geq 0$, with $x = 0$ corresponding to the seafloor trace of the normal fault that shapes the abyssal hill. For simplicity, we assumed that downwarping of the hanging wall produces a topographic low that is instantaneously filled through volcanic extrusion such that $h(x < 0,t)=0$. In Eq. (1), K is the effective diffusivity of topography which depends on topographic gradient:

$$\theta = \tan^{-1}\left(\left|\frac{\partial h}{\partial x}\right|\right), \tag{2}$$

according to the following equation:

$$K = 10^{\left(\log_{10}K_{\min}+\log_{10}\left(\frac{K_{\max}}{K_{\min}}\right)\left(0.5+\left(\frac{1}{\pi}\right)\tan^{-1}\left(\frac{\theta-\theta_c}{w}\right)\right)\right)} \tag{3}$$

In Eq. (3), $K_{\min}$ is the minimum diffusivity at very low gradient and $K_{\max}$ is a maximum value, typically three orders of magnitude greater than $K_{\min}$. This approach keeps diffusivity finite for all gradients and ensures a sharp increase in diffusivity over a narrow range of gradients around the critical angle (θ_c). w acts as a regularization parameter that controls how fast modeled gradients approach θ_c where a larger w means a faster increase towards higher diffusivity at gradients approaching θ_c. In our models, we set θ_c = 35–40° and w = 0.035 and 0.042, respectively.

Tectonic uplift and horizontal advection were parameterized in relation to the horizontal slip rate, U, on the hill-bounding fault. Specifically, we used piece-wise linear functions $v_x(x)$ and $v_z(x)$ that equal zero for all $x \leq 0$, and reach maximum values respectively equal to $U/2$ and $\tan(\theta_F)U/2$ at $x = Ut/2$ (θ_F denotes the dip of the fault). Beyond $x = Ut/2$, $v_x(x)$ is kept constant at $U/2$, and $v_x(x)$ decreases linearly to 0 until x reaches $Ut/2 + S$, where S represents the width of the gently sloping side of the abyssal hill (non-axis-facing). We set $S = 10$ km in our calculations, but note that S has virtually no effect on the morphology of the steep side of the hill (the fault scarp), which was our primary interest. This definition of $v_x(x)$ and $v_z(x)$ captures the uplift, advection, and tilting of abyssal hill topography as the normal fault slips without the complexities related to footwall flexure (e.g., Weissel and Karner 1989). We also assumed a fault dip of $\theta_F = 45°$ (after Thatcher and Hill 1995) for simplicity: U can thus be viewed as a proxy for full heave and throw rate on the fault. Because the model does not account for the subsiding motion of the hanging wall, we assumed the representative

rock uplift rate in the hill is $U/2$, which amounts to assuming symmetric uplift and subsidence in the footwall and hanging wall of a normal fault. To estimate U, we measured the fraction of horizontal extension taken up by faults for each transect. This fraction, F, is classically estimated as the slope of a cumulative fault heave vs. distance to the axis plot (e.g., Searle and Laughton 1977). Multiplying F by the full spreading rate along the transect yields a representative horizontal fault slip rate or uplift rate (adopting a fault dip of 45°), assuming only one fault is active at any given time (e.g., Buck et al. 2005).

Eq. (1) was discretized with a backward-Euler finite difference scheme and solved with Newton iterations to handle the non-linearity of the diffusion law. Advection of topography within the ($v_x(x)$, $v_z(x)$) field is achieved through a particle-in-cell method. We solved Eq. (1) starting from a flat topography to calculate how predefined values of diffusivity (K) and θ_c degrade the interpolated scarp face during fault growth.

3.3. Model results and scarp diffusivity

Our numerical model simulates the evolution of a scarp subjected to diffusive erosion and deposition. Examples are shown in e–h. Early in the simulations, topographic scarps with very small throws are almost instantaneously leveled by diffusion. As a result, they initially develop very gentle slopes even though their underlying fault is steep. When tectonic throw exceeds a characteristic advection-diffusion length ($K / U \sim 10$ m), diffusion no longer keeps up with uplift, and scarp slope increases. This, in turn, increases diffusivity non-linearly, and caps slope at values near the critical angle. Overall, our model reproduces observed trends of increasing scarp slope vs. height which eventually plateau near 30–40° (Fig. 6a).

We compared our simulation results (using the maximum slope measured along modeled scarps) to the moving median of measured slopes with increasing height for scarps within the ~30 km-wide fault growth window (Fig. 6a). Cropping the dataset at <30 km from the axis also partly mitigates any reduction in height or lowering of slopes by pelagic sediment deposition (Fig. 5b). Goodness of fit was assessed through a root-mean-squared (RMS) residual relative to the smoothed median from the slope/height plots (thick red line in Fig. 6a–d). The lower and upper bounds were calculated using the RMS residuals relative to the smoothed 5th and 95th percentiles, respectively (thin red lines in Fig. 6a–d). RMS residuals for each model run are shown in Fig. S4.

Each model run was characterized by an inverse Peclet number Pe^{-1} defined as:

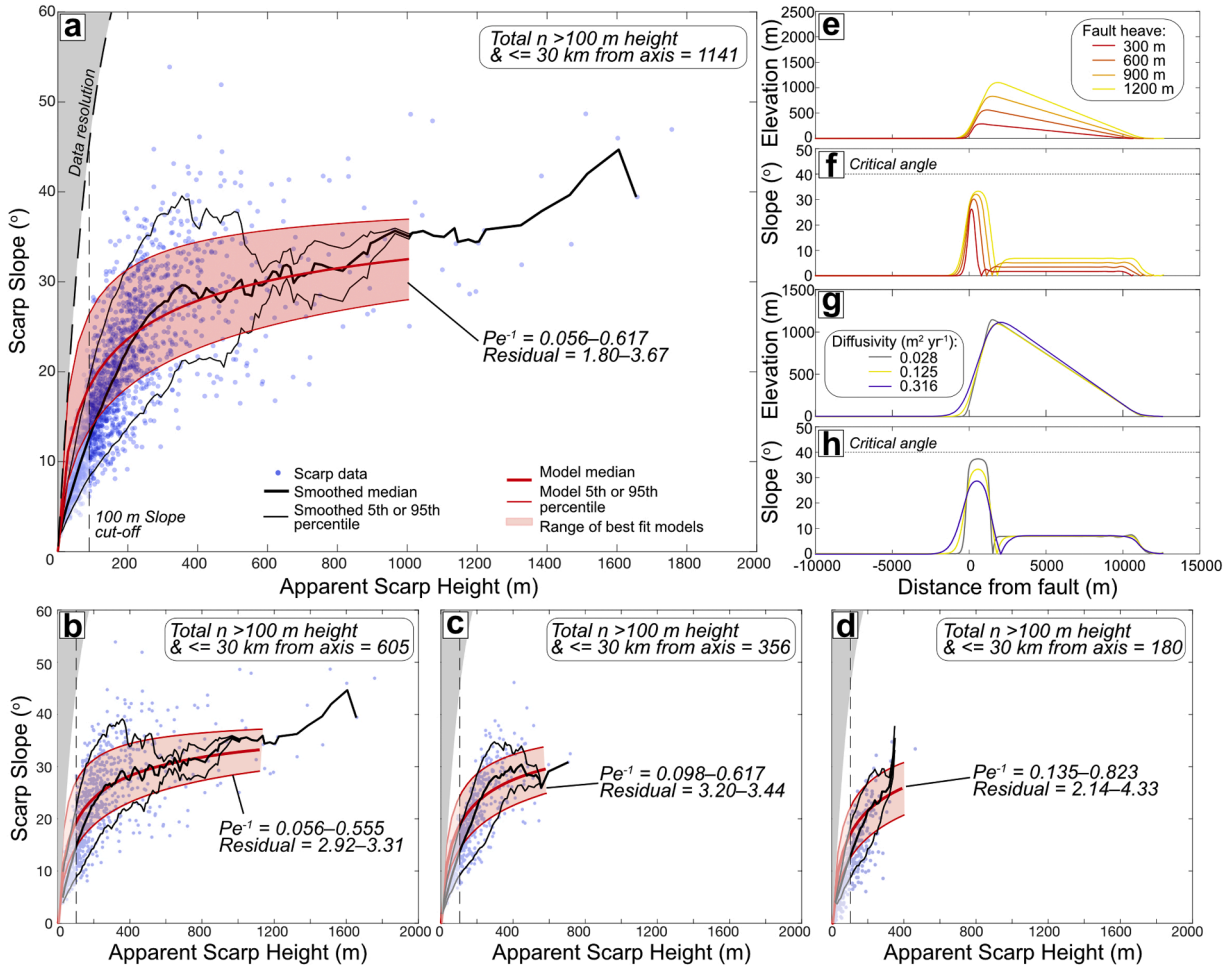

Fig. 6. (a–d) Model results plotted on scarp data for all hills (a), slow (b), intermediate (c), and fast (d) spreading rates. Scarp data comprises abyssal hills <30 km from the ridge axis. Red lines represent the best-fit model runs relative to the median (middle line), 5th (lower line), and 95th (upper line) percentile of the scarp data (black lines). Goodness of fit is based on a root-mean-squared residual relative to the smoothed percentiles from the scarp data. To avoid comparing model results with areas with very few hills, the upper height limit of the red domain is capped at 1100 m for all hills and slow spreading rates, 600 m for intermediate spreading rates, and 400 m for fast ridges. Model parameters are fault dip = 45°, $w = 0.042$, and critical angle (θ_c) = 40° (e-f). Time steps in the modelled evolution of an uplifting abyssal hill for hill height (e) and slope (f) using the same input parameters as parts a–d. (g-h) Morphology of a modeled abyssal hill at ~1100 m height (i.e., limit of red lines in part a) for hill height (g) and slope (h) using different diffusivity. Models use the same input parameters as in (a–d) and a horizontal slip rate of 2.57 mm yr^{-1}.

$$Pe^{-1} = \frac{K}{lU}, \quad (4)$$

where l is a characteristic median scarp height for faults >100 m in height (l = 199 m). This is akin to dimensionless "uplift-erosion numbers" used in a variety of studies that couple tectonics and surface processes (e.g., Olive et al. 2022, Wolf et al. 2022): a large Pe^{-1} means erosion dominates uplift and relief is subdued. To estimate the Pe^{-1} of natural systems, we ran 40 simulations with a broad range of K (0.0003–3 m^2 yr^{-1}, all other parameters kept constant) and report the Pe^{-1} value of the run yielding the lowest RMS misfit of median slope vs. height trends. We note that changing U, w, θ_c, and the subsurface fault dip also affects the final values of Pe^{-1} (Figs. S2, S3). Our chosen parameters are justified in the supplementary materials.

Models indicate that scarp diffusion is relatively inefficient at leveling tectonically induced seafloor uplift, but still represents a significant process that modifies the axis-facing slopes of abyssal hills during fault growth. Pe^{-1} is 0.06–0.82 for faults >100 m in height within 30 km of the ridge axis (range is defined by the 95th and 5th percentile of Pe^{-1}, respectively), with U = 2.57 mm yr^{-1} (average U for all faults >100 m in height) and $\theta_c = 40°$ (Fig. 6a; Table S2). When the same data is binned by spreading rate, Pe^{-1} was 0.06–0.55 for slow (Fig. 6b), 0.10–0.62 for intermediate (Fig. 6c), and 0.14–0.82 for fast spreading rates (Fig. 6d), respectively. Hence, we did not resolve a systematic variation of Pe^{-1} with spreading rate. Results using $\theta_c = 35°$ broadly agree with results using $\theta_c = 40°$ and are presented in the supplementary materials (Table S2).

4. Discussion

4.1. The balance between erosion and uplift

There are possible differences in the tectono-magmatic conditions or seismogenic behavior of abyssal hill-bounding normal faults at different spreading rates (e.g., Frohlich and Wetzel 2007). Nevertheless, to the first order, Pe^{-1} values indicate a similar ratio of erosion to uplift for fast, intermediate, and slow spreading rates (Fig. 7a). This implies that, based on bathymetry derived from shipboard multibeam systems, potential variations in tectono-magmatic processes between spreading rates do not perturb the ratio of erosion to uplift. The results facilitate quantification of bedrock erosion rates for abyssal hills in terms of diffusivity, K, by rearranging Eq. (4):

$$K = \frac{lU}{Pe} \quad (5)$$

For U = 2.57 mm yr^{-1}, l = 199 m (average height for all faults >100 m in height), and the overall Pe^{-1} values of 0.06–0.82, we obtained a K of 0.03–0.42 m^2 yr^{-1} (Table S2). In our model, K scales linearly with U (Eq. (5)) so that individual K values only apply to a specific fault slip rate. Accordingly, we can use the full range of U from the transects measured here (0.72–9.25 mm yr^{-1}; Fig. 8a) to scale the smallest and largest K values derived from the median U. The resulting overall K using the full range of U is 0.01–1.51 m^2 yr^{-1}. This range is comparable to gravity driven failure and turbidity flows of pelagic sediment from the MAR, which range from 0.04 to 1.00 m^2 yr^{-1} (Fig. 7b; Mitchell, 1995; Webb and Jordan, 2001).

The values of U for each transect do not support a systematic variation in fault slip rate, and therefore K, for different MOR spreading rates (Fig. 8a). U ranges from 0.72 to 9.25 mm yr^{-1} with a large spread encompassing most of this range for all spreading rates (Fig. 8a). Previous estimates of growth rates for abyssal hill faults based on the height and spacing of faults are 1–2 mm yr^{-1} from the slow spreading MAR (McAllister and Cann, 1996) and 6–8 mm yr^{-1} from the EPR (Cowie et al., 1993). Our dataset shows a data gap for slow spreading faults with high fault growth rates (Fig. 8a). This gap could be filled by accretion dominated by detachment faulting, which we excluded from our analysis. In such terrains, detachments may accommodate most of the spreading resulting in elevated uplift rates like the >7 mm yr^{-1} suggested at the Atlantis Massif on the slow-spreading Mid-Atlantic ridge (Fig. 8a; Escartín et al., 2022). We note that U values calculated here and fault growth rates from the literature do not account for processes such as partial or complete scarp burial by sedimentation or by volcanic deposits (e.g., Webb and Jordan 2001, Escartín et al. 2007). Moreover, these growth rates are a high end-member because we assume only one fault is active at a time (Buck et al., 2005). The fault growth window is on the order of 10 to a few 10 s of km, so several faults may be active simultaneously for fault spacings <10 km. Hence, we cannot argue for systematic variation in uplift rate with spreading rates.

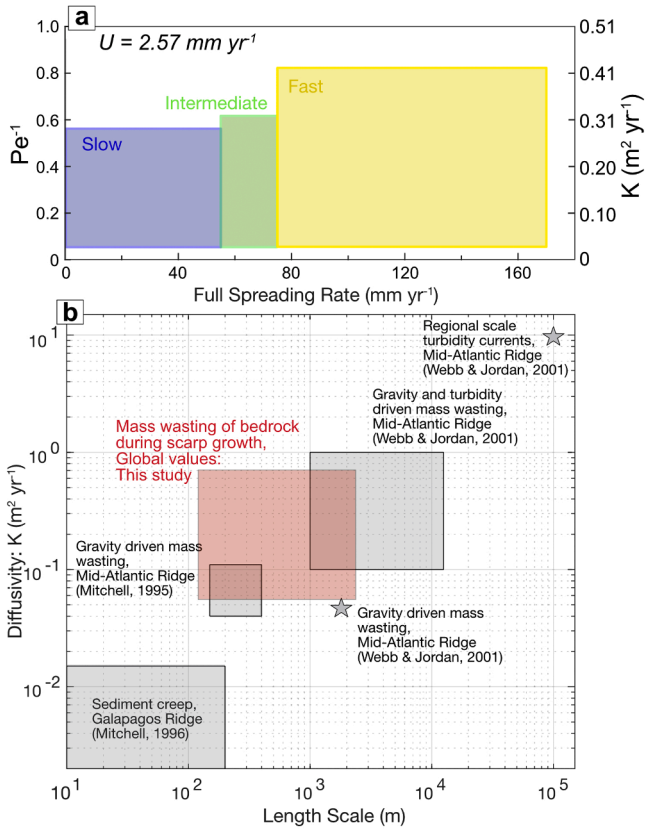

Fig. 7. (a) Plot of inverse Peclet number (Pe^{-1}) and diffusivity (K) with increasing spreading rate. The colored boxes represent the spreading rates bounds (slow = <55 mm yr^{-1}, intermediate = 55–75 mm yr^{-1}, and fast = >75 mm yr^{-1}) and the 5th and 95th percentiles of Pe^{-1} or K for a given uplift or horizontal slip rate (U) (assuming a fault dip of 45°). The boxes assume U = 2.57 mm yr^{-1} based on the median U for faults >100 m in height. (b) Comparison of bedrock K calculated in this study with K for erosion of pelagic sediment over different length scales (amended from Webb and Jordan 2001). The black boxes represent ranges of uncertainty whereas stars have no uncertainty. The red box is bounded by the minimum and maximum K values (using U = 0.72 & 9.25 mm yr^{-1}), and we define the length scale using fault heave with a minimum of 100 m and a maximum of 1750 m.

Our analysis has certain limitations. We note that the morphological evolution documented in Fig. 3 is heavily weighted towards slow spreading ridges, because scarps >100 m high are most abundant at slow rates and scarce at fast rates (n = 2258, 584, and 674 for slow, intermediate, and fast, respectively). Where possible, our analysis focused on areas with higher data density. For example, we only compared abyssal hills <1100 m tall at slow spreading rates with our model results to avoid the sparse data coverage above 1100 m height (Fig. 6b). Due to the low scarp heights at fast spreading ridges (n = 180 > 100 m in height and <30 km from the axis), the trend of the smoothed median line in Fig. 6d is poorly constrained beyond ~300 m in height.

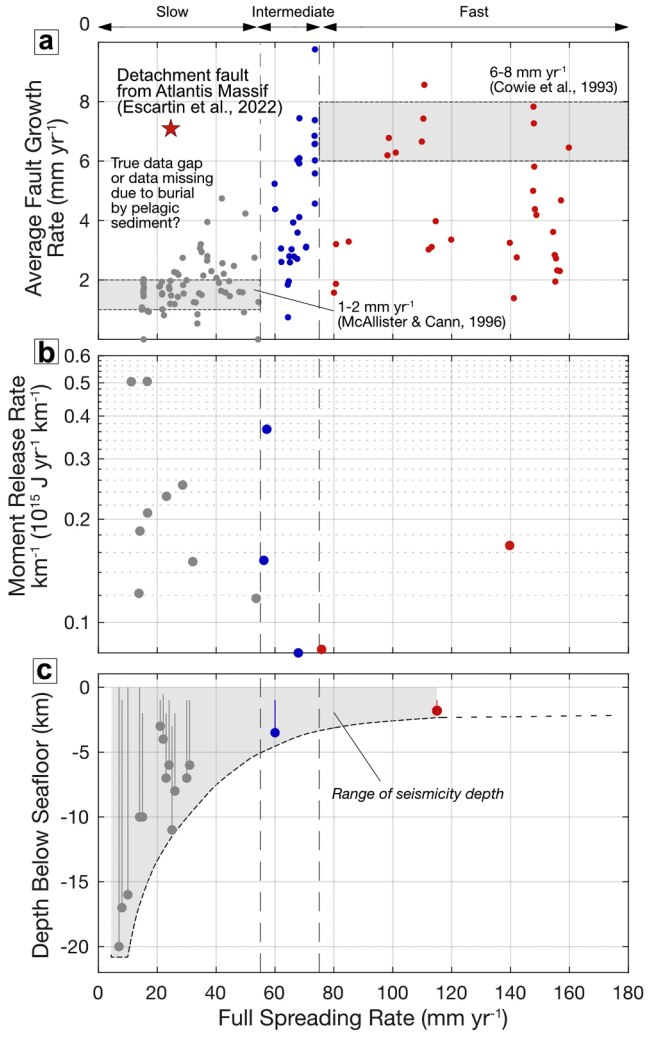

Fig. 8. (a) Minimum fault growth rates versus spreading rate for every transect measured here. The grey boxes are ranges of previously published estimates for fault growth rates based on the references shown here. (b) Seismic moment release rates from Frohlich and Wetzel (2007) normalized by ridge axis length. Data provided in Table S3. (c) Depth range of microseismicity across spreading rates. References and data for part c are included in Table S4.

Therefore, the calibration of Pe^{-1} against data is limited at fast-spreading sites and the range of Pe^{-1} of 0.14–0.82 for fast faults is less robust than for faults developing at slower-spreading ridges (Fig. 6b–c).

4.2. Processes driving mid-ocean ridge mass wasting

4.2.1. Earthquake controls on erosion during scarp growth

Like terrestrial settings, if earthquakes are an important driver of abyssal hill bedrock erosion, then spatial variation in earthquake ground accelerations should be an important control on patterns in mass wasting (e.g., Croissant et al. 2019, Medwedeff et al. 2020). In simplest terms, ground acceleration depends on earthquake magnitude, depth, hypocentral distance, and the shear wave velocity of shallow bedrock (e.g., Abrahamson and Silva 1997). In theory, differences in seismic behavior at different spreading rates should modify erosion parameters. To understand mass wasting behavior at different spreading rates requires an examination of how seismic parameters vary for different spreading rates.

Seismic moment release and coupling are both thought to decrease with increasing spreading rate (Cowie et al., 1993; Frohlich and Wetzel, 2007; Mark et al., 2018). However, the normalization of the total seismic energy by distance along the ridge axis varies greatly at slow spreading ridges, covering the overall trend across spreading rates (Fig. 8b). A similar trend is observed for the depth of micro-seismicity, although these experiments have limited spatial and temporal extents (Fig. 8c). Shallow micro-seismicity is observed at all ridges, but deep micro-seismicity (e.g., >5–6 km) is only recorded at slow spreading rates (Fig. 8c). Consequently, we speculate that while seismicity may be less frequent with slightly lower energy release at fast spreading ridges, the seismicity may be concentrated at shallow depths and result in similar ground shaking compared to slow spreading ridges. Similar average ground shaking for different spreading rates, despite possible variations in seismic parameters, could be one factor that accounts for the similarity in Pe^{-1} across spreading rates.

Seismicity at MORs occurs mostly within a few tens of kilometers of the ridge axis. The overall frequency of earthquakes measured with hydrophone arrays from the Mid-Atlantic Ridge (MAR) and the Southwest Indian Ridge (SWIR) is greatest within 10–20 km of the ridge axis and gradually decreases away from the axis with infrequent earthquakes occurring up to 200 km from the axis (Fig. 4a; Smith et al., 2003; Tsang-hin-sun et al., 2016). These seismicity observations are consistent with previous estimations for the width of the fault growth window (Table S1). Previous estimates are derived from the distribution of seismicity or indirectly from the evolution of fault parameters (spacing, height) and the distance from the axis at which these stabilize (Table S1). A 20–30 km limit for the fault growth window is broadly consistent with the pronounced increase in height of the largest scarps within 10 km of the ridge axis (Fig. 4b). We note that only ~15 % of all abyssal hills in our dataset are within 40 km of a transform fault, so transform seismicity is not considered to be a major contributor to abyssal-hill slope degradation here.

The documentation of fresh bedrock talus at the ridge axis in sidescan sonar data (Fig. 2a) and near-bottom bathymetry surveys (Fig. S1) supports scarp average slopes being degraded via bedrock mass wasting within the fault growth window. Shipboard bathymetry and AUV sidescan sonar data from the Southeast Indian Ocean collected as part of the search for Malaysian Airlines flight MH370 (AusSeabed Marine Data Portal at: https://portal.ga.gov.au/persona/marine) constitute a substantial dataset to evaluate bedrock mass wasting outside the fault growth window. From data between 350 and 2500 km from the axis, we identified possible thin fingers of fresh bedrock talus at the foot of abyssal hill-bounding faults in just two out of 66 abyssal hills examined from a study area of ~98,000 km^2 (Fig. 9; methods in the supplementary materials).

The few observations of potential fresh talus at 350–2500 km from the axis indicates that bedrock mass wasting is extremely rare far off axis. Other seafloor geomorphic studies also report little evidence for fresh talus >30 km off axis at fast and slow spreading rates (e.g., Macdonald and Luyendyk 1985, Escartín et al., 1999). The sidescan sonar data from the Southeast Indian Ocean records widespread low reflectivity seafloor, which indicates widespread sediment cover (Fig. 9). Limited bedrock talus and widespread sediment deposition are consistent with the levelling off in the 95th percentile of height and slope beyond ~500 km off-axis (Fig. 3). Seismicity is also limited away from the ridge axis. Only two earthquakes were recorded in the deep-tow sonar survey area for the Southeast Indian Ocean between 1950 and 2021 (https://earthquake.usgs.gov/data/comcat/; Fig. 9a). These combined off-axis morphological and seismological observations indicate that bedrock mass wasting is not significant beyond ~30 km off axis and highlight the importance of coseismic shaking as a trigger for mass wasting near-axis.

4.2.2. Alteration processes

Alteration may also facilitate mass wasting during scarp growth. Bedrock alteration (e.g., serpentinization, clay formation) and possibly fluid flow (changes in pore fluid pressure), can reduce the internal friction and shear strength of the bedrock and, theoretically, promote

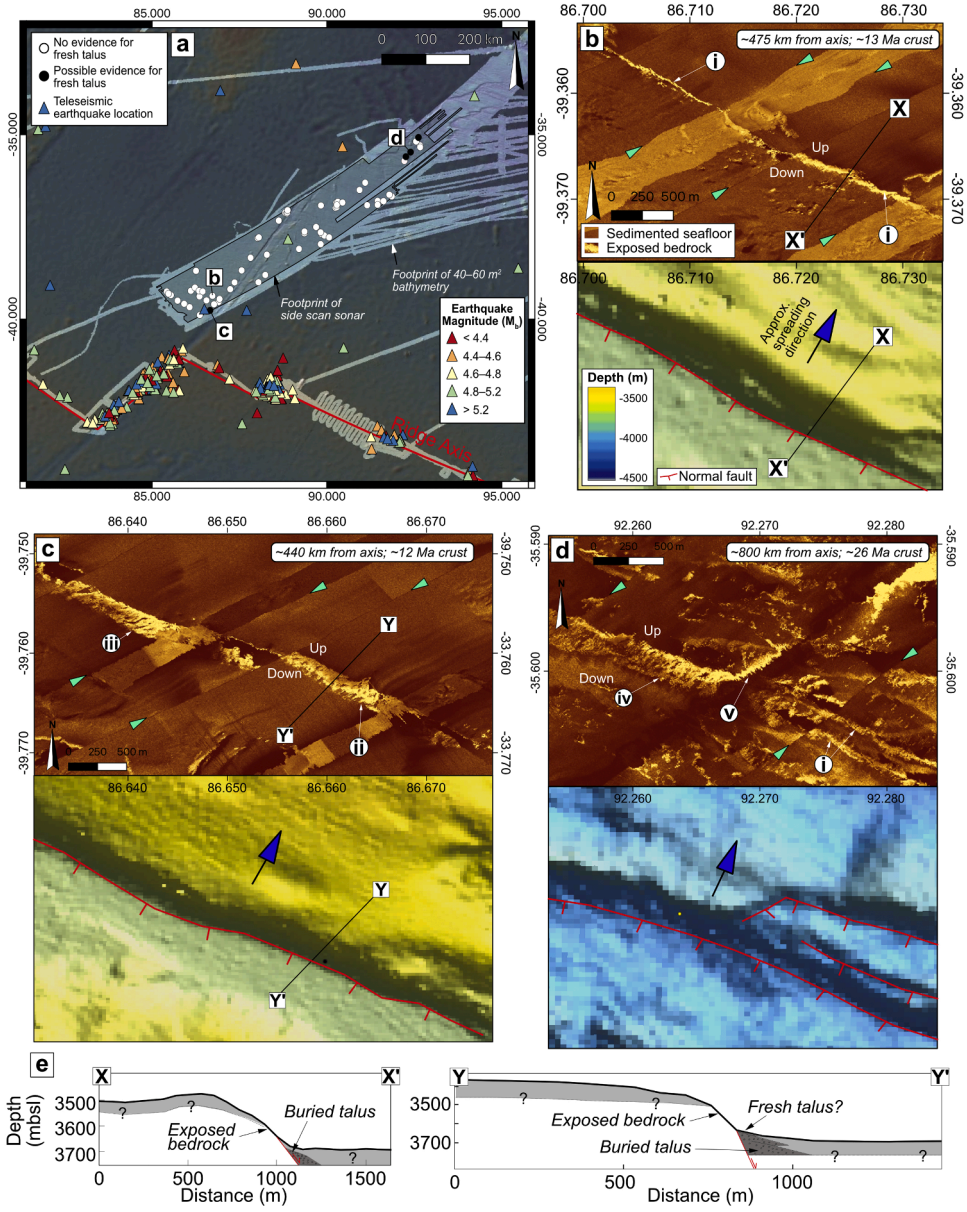

Fig. 9. Side scan sonar (5 m horizontal resolution) and bathymetry data (40–60 m horizontal resolution) from the Southeastern Indian Ocean. (a) Map locating the data relative to the Southeast Indian Ridge axis (location of (a) is shown in Fig. 1a). Earthquakes are from the USGS Advanced National Seismic System Comprehensive Earthquake Catalog (U.S. Geological Survey 2017) for earthquakes > M_b 2.5 from 1950 to the present. (b–d) AUV side scan sonar data (top) above corresponding shaded relief, ship-board, bathymetry (bottom) covering the same area. Roman numerals represent features of interest described here. In the sonar data sedimented seafloor is darker brown or orange whereas exposed bedrock is pale brown or yellow. (b) Representative abyssal hill. i: smooth, linear contact between sediment and bedrock indicates no recent mass wasting. (c) Isolated abyssal hill with possible recent bedrock mass wasting. ii: Possible fingers of fresh talus. iii: Sedimented talus. (d) A relay zone. iv: Possible recent bedrock mass wasting which could also be sedimented talus. v: Chutes or fingers of talus on the relay scarp. (e) Bathymetric profiles across X-X' and Y-Y' from (b) and (c). Pale grey domain sketches extent of pelagic sediment and dark grey is schematic talus. Bathymetry and sonar data are from Geoscience Australia. Sonar maps show artifacts indicated by green arrows and that generally run WSW-ENE (nadir of sonar swath, differences in absolute acoustic backscatter across adjacent tracks, mosaicking seams).

erosion (Tucholke et al., 1997). Bedrock alteration is thought to occur primarily at and in the vicinity of the ridge axis during exhumation (e.g., Cannat et al. 2010, Merdith et al. 2020). The degree of off-axis, shallow, bedrock alteration depends on sediment cover. Fluid ingress and egress, and accompanying bedrock alteration may preferentially occur at un-sedimented bathymetric highs with seafloor bedrock exposures (Fig. 9; Coogan and Gillis, 2018). If alteration gradually weakens bedrock and promotes mass wasting, then an increase in the frequency of mass wasting with distance from the axis would be expected along with the corresponding evolution in abyssal hill morphology. The limited bedrock mass wasting documented outside of the fault growth window (Fig. 9), coupled with a leveling off in scarp height and slope >500 km off axis (Fig. 3), indicate that any potential long-term bedrock alteration does not noticeably enhance mass wasting.

Conversely, alteration processes like mineral precipitation, may stabilize bedrock and reduce the potential for mass wasting. Palagonitization, for example, can increase the density and decrease the porosity and permeability of basalt (e.g., Weaver et al., 2020). We speculate that crack closure or surface precipitation may locally increase the internal friction of oceanic bedrock with a stabilizing effect acting against any potential alteration weakening. This is supported by subsurface geophysical observations. A rapid increase in seismic velocity at the top

of layer 2 from 3.0 km s^{-1} at 0 Ma to 4.6 km s^{-1} at 10.5 Ma followed by a more gradual increase to 5.0 km s^{-1} at 170 Ma has been attributed to precipitation of hydrothermal alteration products within cracks (Christeson et al., 2019). Consequently, any potential weakening from alteration may be partially offset by strengthening from mineralization. Either way, based on the observations above, we suggest the primary trigger for bedrock mass wasting is coseismic shaking during scarp growth near-axis.

4.3. Global mass flux on abyssal hill

To assess the global significance of abyssal hill mass wasting in term of detrital sediment fluxes, we quantified the erosional mass flux of bedrock associated with the growth of the largest abyssal hills. We calculated the average annual mass flux for an abyssal hill (Q_{ave}) using the average area eroded and corresponding growth time for a representative large abyssal hill (i.e., 200 m tall; Fig. S8). Next, we multiplied Q_{ave} by the total length of the global MOR system of 60,000–70,000 km assuming only one abyssal hill is active per cross-axis transect. For a typical hill spacing of 3 km (from our global dataset) and a cross-axis width of 60 km for the fault growth window, we calculate that 20 abyssal hills are active in one cross-axis transect. Therefore, by multiplying the number of active abyssal hills by Q_{ave} and considering all uncertainties, we calculate an annual earthquake-induced abyssal hill mass flux of 24–1428 million m^3 yr^{-1}. We verified our calculation based on model outputs with an alternative approach using simple trigonometry (full details on all calculations in the supplementary materials). This value records the combined effects of near-axis fault growth and erosion, with the associated uncertainties, and excludes other mass wasting environments (e.g., transform- and non-transform scarps, detachment-dominated seafloor, flanks of seamounts and volcanic islands, etc.).

For comparison, the total global mass flux from earthquake-induced terrestrial landslides is estimated at 16.8–22.4 billion m^3 yr^{-1} (Broeckx et al., 2020). While up to two orders of magnitude less than subaerial sites, the total earthquake-induced, abyssal-hill, mass wasting is still a significant surface process shaping the oceanic crust, especially given the process is concentrated along a narrow strip of seafloor. Mass wasting denuding the oceanic lithosphere may impact alteration and modulate chemical fluxes between the lithosphere and the ocean (e.g., Merdith et al. 2020). Further investigations into submarine mass wasting are required to study its impact on weathering fluxes (Isson et al., 2020), on seafloor ecosystems (Stefanoudis et al., 2016), and on the safety of submarine infrastructure and resource extraction (Smith et al., 2018). Finally, complete quantification of ocean seafloor mass wasting should include other sites. Transform faults have cumulative lengths on the order of a third of the global MOR system, and are typically more seismically-active than their adjacent ridge segments. Transforms may thus increase the global mass flux of bedrock erosion by an amount commensurable to ridges. Intraplate volcanoes and seamounts are also ubiquitous and show pervasive, albeit unquantified, flank erosion (e.g., Mitchell et al. 2003).

4.4. Growth and decay of abyssal hills

Based on the morphological and seismological data presented here, we posit that the overall morphology of abyssal hills is established by simultaneous tectonic rock uplift and coseismic bedrock mass wasting during fault growth (Fig. 10). A rapid increase in height for young scarps within the fault growth window is accompanied by a simultaneous reduction in slope below the assumed fault dip of 45–60° (Fig. 4c). As faults are rafted off-axis, the draping and redistribution of pelagic sediments by turbidity currents and sediment mass wasting smooths topography (Webb and Jordan, 2001; Tominaga et al., 2011). This is reflected in gentler slopes for a given height for abyssal hills >20 Ma compared to abyssal hills <20 Ma (Fig. 5b). Sediment accumulation at the foot of scarps can potentially explain the gradual decrease in the 95th percentile for scarp height and slope away from the ridge axis, although the data is somewhat noisy (Fig. 3c–d). Isolated earthquakes and, possibly, isolated bedrock mass wasting, may occasionally occur outside of the fault growth window (e.g., Bergman and Solomon 1984;

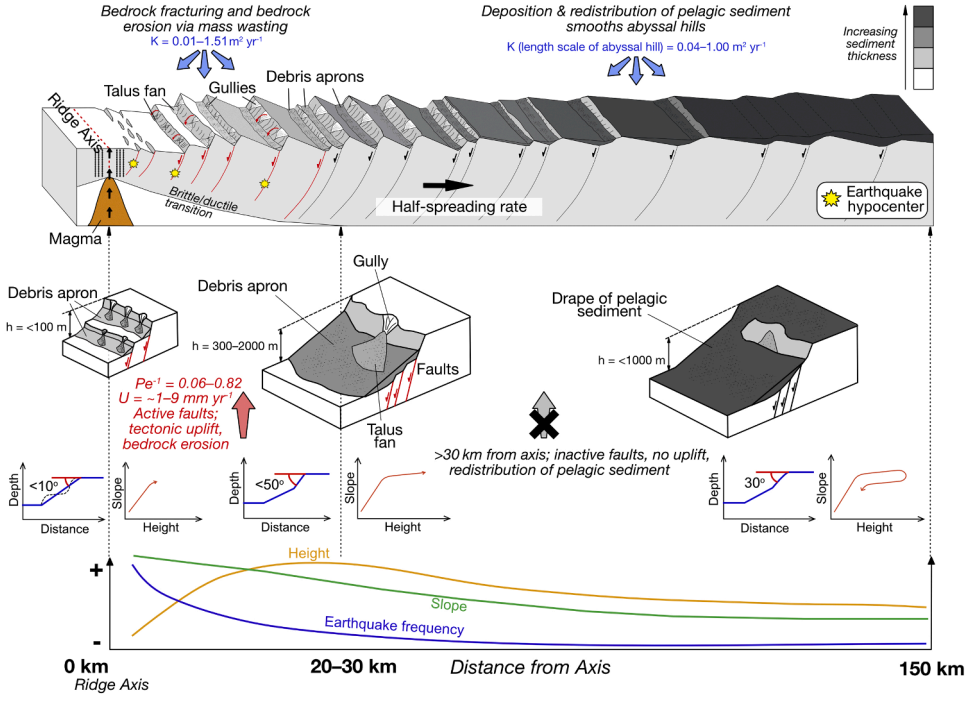

Fig. 10. Summary of the morphological evolution of mid-ocean ridge fault scarps and abyssal hills with increasing distance from the ridge axis. The geomorphic data and model results presented in this study allow us to add quantitative bedrock erosion parameters to previously existing tectonic models of abyssal hill evolution. All values are from this study except the diffusivity value for pelagic sediment, which is from Webb and Jordan (2001). The block models are amended from Allerton et al. (1995). Faults in red are potentially active and faults in black are inactive.

Figs. 4a, 10). However, the overall decreasing trend in the 95th percentile of height and slope off axis indicates that these isolated events do not promote scarp growth, at least at the resolution of our data (Figs. 5b, 10).

5. Conclusion

We compiled a global database on abyssal hill morphology derived from shipboard bathymetry data. The resulting data support a model in which coseismic shaking is the primary trigger for mass wasting events that reshape growing abyssal hills. For the tallest abyssal hills (>100 m), height increases rapidly, but scarp slopes are generally degraded to <30° within 10 km of the ridge axis compared to an original underlying fault dip of 45–60°. The rapid decrease in scarp slope during initial growth records the cumulative effect of discrete coseismic mass wasting events. This result demonstrates that abyssal hill scarp degradation is active from fault inception at the ridge axis. Beyond 20–30 km from the ridge axis, seismogenic fault growth ceases and there is minimal bedrock erosion. A gradual decrease in both the height and slope of the tallest scarps beyond 30 km from the axis is attributed to the gentle smoothing of topography via the blanketing and redistribution of pelagic sediment.

We used numerical modelling and the global database of abyssal hill morphology to quantify how cumulative coseismic erosion controls the morphology of abyssal hills. The results show that erosion is relatively inefficient at leveling abyssal hills, but still profoundly reduces their slopes. The balance between erosion and uplift is similar for slow, intermediate, and fast spreading rates, as expressed by the uplift-erosion number Pe^{-1}, which ranges from 0.06 to 0.82 with no discernable trend across spreading rates. Our results also provide the first constraint on bedrock scarp diffusivity with rates ranging from 0.01 to 1.51 m^2 yr^{-1}. This study demonstrates that mass wasting during abyssal hill growth is a significant surface process operating along the global MOR system and provides a framework to incorporate bedrock mass wasting into future models of landscape evolution in actively uplifting extensional settings.

CRediT authorship contribution statement

Alex Hughes: Writing – original draft, Visualization, Methodology, Investigation, Formal analysis, Data curation, Conceptualization. **Jean-Arthur Olive:** Writing – review & editing, Writing – original draft, Visualization, Methodology, Investigation, Formal analysis, Conceptualization. **Luca C. Malatesta:** Writing – review & editing, Visualization, Methodology, Conceptualization. **Javier Escartín:** Writing – review & editing, Supervision, Methodology, Investigation, Funding acquisition, Conceptualization.

Declaration of competing interest

The authors declare that they have no known competing financial interests or personal relationships that could have appeared to influence the work reported in this paper.

Acknowledgments

All shipboard bathymetry data used in this study was downloaded from the Global Multi-Resolution Topography Data Synthesis [GMRT] available at: https://www.gmrt.org/index.php (Ryan et al., 2009). Near-bottom bathymetry used in Figs. 1 and S1 were downloaded from the Marine Geosciences Data System available at: https://www.marine-geo.org/index.php. Shipboard bathymetry and sidescan sonar data used for Fig. 9 were collected as part of the search for Malaysian Airlines flight MH370 and are publicly available from the AusSeabed Marine Data Portal at: https://portal.ga.gov.au/persona/marine. This work was supported by the ANR project SERSURF (PI J. Escartín, ANR-17-CE31–0020) and the Pacific Rim Ocean Data Mobilization and Technology (PRODIGY) program. This manuscript greatly benefitted from constructive in-depth reviews by J. Goff and N. Mitchell.

Supplementary materials

Supplementary material associated with this article can be found, in the online version, at doi:10.1016/j.epsl.2024.119073.

Data availability

All data generated for this study is presented in the main text or is available in the supplement.

References

Alexander, R.T., Macdonald, K.C., 1996. Sea Beam, SeaMARC II and ALVIN-based studies of faulting on the East Pacific Rise 9° 20′ N–9° 50′ N. Mar. Geophys. Res. 18, 557–587 (Dordr).

Allerton, S., Murton, B.J., Searle, R.C., Jones, M., 1995. Extensional faulting and segmentation of the Mid-Atlantic Ridge north of the Kane Fracture Zone (24° 00′ N to 24° 40′ N). Mar. Geophys. Res. 17 (1), 37–61. https://doi.org/10.1007/BF01268050 (Dordr).

Abrahamson, N.A., Silva, W.J., 1997. Empirical response spectral attenuation relations for shallow crustal earthquakes. Seismol. Res. Lett. 68 (1), 94–127.

Behn, M.D., Ito, G., 2008. Magmatic and tectonic extension at mid-ocean ridges: 1. Controls on fault characteristics. Geochem. Geophys. Geosyst. 9 (8).

Bergman, E.A., Solomon, S.C., 1984. Source mechanisms of earthquakes near mid-ocean ridges from body waveform inversion: implications for the early evolution of oceanic lithosphere. J. Geophys. Res. 89, 11415–11441.

Bird, P., 2003. An updated digital model of plate boundaries. Geochem. Geophys. Geosyst. 4 (3).

Bohnenstiehl, D.W.R., Carbotte, S.M., 2001. Faulting patterns near 19°30′S on the East Pacific Rise: fault formation and growth at a superfast spreading center. Geochem. Geophys. Geosyst. 2 (9). https://doi.org/10.1029/2001GC000156.

Broeckx, J., Rossi, M., Lijnen, K., Campforts, B., Poesen, J., Vanmaercke, M., 2020. Landslide mobilization rates: a global analysis and model. Earth Sci. Rev. 201, 102972. https://doi.org/10.1016/j.earscirev.2019.102972 (September 2019).

Buck, W.R., Lavier, L.L., Poliakov, A.N., 2005. Modes of faulting at mid-ocean ridges. Nature 434 (7034), 719–723.

Cannat, M., Mangeney, A., Ondréas, H., Fouquet, Y., Normand, A., 2013. High-resolution bathymetry reveals contrasting landslide activity shaping the walls of the Mid-Atlantic Ridge axial valley. Geochem. Geophys. Geosyst. 14 (4), 996–1011. https://doi.org/10.1002/ggge.20056.

Cannat, M., Fontaine, F., Escartin, J., 2010. Serpentinization and associated hydrogen and methane fluxes at slow spreading ridges. Diversity of hydrothermal systems on slow spreading ocean ridges. Geophys. Monogr. Ser. 188, 241–264.

Christeson, G.L., Goff, J.A., Reece, R.S., 2019. Synthesis of oceanic crustal structure from two-dimensional seismic profiles. Rev. Geophys. 57, 504–529. https://doi.org/10.1029/2019RG000641.

Coogan, L.A., Gillis, K.M., 2018. Low-temperature alteration of the seafloor: impacts on ocean chemistry. Ann. Rev. Earth Planet. Sci. 46 (1), 21–45.

Cowie, P.A., Scholz, C.H., Edwards, M., Malinverno, A., 1993. Fault strain and seismic coupling on mid-ocean ridges. J. Geophys. Res. 98 (B10). https://doi.org/10.1029/93jb01567.

Croissant, T., Steer, P., Lague, D., Davy, P., Jeandet, L., Hilton, R.G., 2019. Seismic cycles, earthquakes, landslides and sediment fluxes: linking tectonics to surface processes using a reduced-complexity model. Geomorphology 339, 87–103.

Densmore, A.L., Anderson, R.S., McAdoo, B.G., Ellis, M.A., 1997. Hillslope evolution by bedrock landslides. Science 275 (5298), 369–372. https://doi.org/10.1126/science.275.5298.369 (1979).

Deffeyes, K.S., 1970. The axial valley: a steady state feature in the terrain. In: Johnson, J., Smith, B.C. (Eds.), Megatectonics of Continents and Oceans. Rutgers Univ. Press, pp. 194–222.

Dick, H.J., Lin, J., Schouten, H., 2003. An ultraslow-spreading class of ocean ridge. Nature 426 (6965), 405–412. https://doi.org/10.1038/nature02128.

Escartín, J., Cowie, P.A., Searle, R.C., Allerton, S., Mitchell, N.C., MacLeod, C.J., Slootweg, A.P., 1999. Quantifying tectonic strain and magmatic accretion at a slow spreading ridge segment, Mid-Atlantic Ridge, 29° N. J. Geophys. Res. Solid Earth 104 (B5), 10421–10437.

Escartín, J., Soule, S.A., Fornari, D.J., Tivey, M.A., Schouten, H., Perfit, M.R., 2007. Interplay between faults and lava flows in construction of the upper oceanic crust: the East Pacific Rise crest 9°25′-9°58′N. Geochem. Geophys. Geosyst. 8 (6). https://doi.org/10.1029/2006GC001399.

Escartín, J., Smith, D.K., Cann, J., Schouten, H., Langmuir, C.H., Escrig, S., 2008. Central role of detachment faults in accretion of slow-spreading oceanic lithosphere. Nature 455 (7214), 790–794.

Escartín, J., John, B., Cannat, M., Olive, J.A., Cheadle, M., Früh-Green, G., Cotterill, C., 2022. Tectonic termination of oceanic detachment faults, with constraints on tectonic uplift and mass wasting related erosion rates. Earth Planet. Sci. Lett. 584, 117449.

Frohlich, C., Wetzel, L.R., 2007. Comparison of seismic moment release rates along different types of plate boundaries. Geophys. J. Int. 171 (2), 909–920. https://doi.org/10.1111/j.1365-246X.2007.03550.x.
Goff, J.A., 1991. A global and regional stochastic analysis of near-ridge abyssal hill morphology. J. Geophys. Res. 96 (B13). https://doi.org/10.1029/91jb02275.
Goff, J.A., Ma, Y., Shah, A., Cochran, J.R., Sempéré, J.C., 1997. Stochastic analysis of seafloor morphology on the flank of the Southeast Indian Ridge: the influence of ridge morphology on the formation of abyssal hills. J. Geophys. Res. Solid Earth 102 (B7), 15521–15534.
Goff, J.A., Tucholke, B.E., 1997. Multiscale spectral analysis of bathymetry on the flank of the Mid-Atlantic Ridge: modification of the seafloor by mass wasting and sedimentation. J. Geophys. Res. 102, 15447–15462.
Goff, J.A., 2020. Identifying characteristic and anomalous mantle from the complex relationship between abyssal hill roughness and spreading rates. Geophys. Res. Lett. 47. https://doi.org/10.1029/2020GL088162 e2020GL088162.
Hilley, G.E., Sare, R.M., Aron, F., Baden, C.W., Caress, D.W., Castillo, C.M., Dobbs, S.C., Gooley, J.T., Johnstone, S.A., Liu, F., McHargue, T., 2020. Coexisting seismic behavior of transform faults revealed by high-resolution bathymetry. Geology 48 (4), 379–384.
Hovius, N., Meunier, P., Lin, C.W., Chen, H., Chen, Y.G., Dadson, S., et al., 2011. Prolonged seismically induced erosion and the mass balance of a large earthquake. Earth Planet. Sci. Lett. 304 (3–4), 347–355. https://doi.org/10.1016/j.epsl.2011.02.005.
Howell, S.M., Ito, G., Behn, M.D., Martinez, F., Olive, J.A., Escartín, J., 2016. Magmatic and tectonic extension at the Chile Ridge: evidence for mantle controls on ridge segmentation. Geochem. Geophys. Geosyst. 17 (6), 2354–2373. https://doi.org/10.1002/2016GC006380.
Hughes, A., Escartín, J., Olive, J.A., Billant, J., Deplus, C., Feuillet, N., et al., 2021. Quantification of gravitational mass wasting and controls on submarine scarp morphology along the Roseau Fault, Lesser Antilles. J. Geophys. Res. Earth Surf. 126 (4), 1–25. https://doi.org/10.1029/2020JF005892.
Hughes, A., Escartín, J., Billant, J., Leclerc, F., Andreani, M., Olive, J.A., Arnaubec, A., Dano, A., Delorme, A., Deplus, C., Feuillet, N., et al., 2023. Seafloor earthquake ruptures and mass wasting from the 2004 Mw 6.3 Les Saintes submarine earthquake. Commun. Earth Environ. 4 (1), 270.
Isson, T.T., Planavsky, N.J., Coogan, L.A., Stewart, E.M., Ague, J.J., Bolton, E.W., Zhang, S., McKenzie, N.R., Kump, L.R., 2020. Evolution of the global carbon cycle and climate regulation on earth. Glob. Biogeochem. Cycles 34 (2), e2018GB006061.
Le Saout, M., Thibaud, R., Gente, P, 2018. Detailed analysis of near tectonic features along the East Pacific Rise at 16°N, near the Mathematician hot spot. J. Geophys. Res. Solid Earth 123 (6), 4478–4499. https://doi.org/10.1029/2017JB015301.
Macdonald, K.C., Luyendyk, B.P., 1985. Investigation of faulting and abyssal hill formation on the flanks of the East Pacific Rise (21 N) using Alvin. Mar. Geophys. Res. 7 (4), 515–535 (Dordr).
Macdonald, K.C., Fox, P.J., Alexander, R.T., Pockalny, R., Gente, P., 1996. Volcanic growth faults and the origin of Pacific abyssal hills. Nature 380 (6570), 125–129.
Malamud, B.D., Turcotte, D.L., Guzzetti, F., Reichenbach, P., 2004. Landslides, earthquakes, and erosion. Earth Planet. Sci. Lett. 229 (1–2), 45–59. https://doi.org/10.1016/j.epsl.2004.10.018.
Mark, H.F., Behn, M.D., Olive, J.-A., Liu, Y., 2018. Controls on mid-ocean ridge normal fault seismicity across spreading rates from rate-and-state friction models. J. Geophys. Res. Solid Earth 123, 6719–6733. https://doi.org/10.1029/2018JB015545.
McAllister, E., Cann, J.R., 1996. Initiation and evolution of boundary-wall faults along the Mid-Atlantic Ridge, 25-29°N. Geol. Soc. Spec. Publ. 118 (118), 29–48. https://doi.org/10.1144/GSL.SP.1996.118.01.03.
Medwedeff, W.G., Clark, M.K., Zekkos, D., West, A.J., 2020. Characteristic landslide distributions: an investigation of landscape controls on landslide size. Earth Planet. Sci. Lett. 539, 116203.
Merdith, A.S., del Real, P.G., Daniel, I., Andreani, M., Wright, N.M., Coltice, N., 2020. Pulsated global hydrogen and methane flux at mid-ocean ridges driven by Pangea breakup. Geochem. Geophys. Geosyst. 21. https://doi.org/10.1029/2019GC008869 e2019GC008869.
Mills, M.M., Pappalardo, R.T., Panning, M.P., Leonard, E.J., Howell, S.M., 2023. Moonquake-triggered mass wasting processes on icy satellites. Icarus 399, 115534.
Mitchell, N.C., 1995. Diffusion transport model for pelagic sediments on the Mid-Atlantic Ridge. J. Geophys. Res. 100 (B10). https://doi.org/10.1029/95jb01974.
Mitchell, N.C., 1996. Creep in pelagic sediments and potential for morphologic dating of marine fault scarps. Geophys. Res. Lett. 23 (5), 483–486. https://doi.org/10.1029/96GL00421.
Mitchell, N.C., Tivey, M.A., Gente, P., 2000. Seafloor slopes at mid ocean ridges from submersible observations and implications for interpreting geology from seafloor topography. Earth Planet. Sci. Lett. 183 (3–4), 543–555. https://doi.org/10.1016/S0012-821X(00)00270-3.
Mitchell, N.C., Dade, W.B., Masson, D.G., 2003. Erosion of the submarine flanks of the Canary Islands. J. Geophys. Res. Earth Surf. 108 (F1).
Olive, J.A., Behn, M.D., Ito, G., Buck, W.R., Escartín, J., Howell, S., 2015. Sensitivity of seafloor bathymetry to climate-driven fluctuations in mid-ocean ridge magma supply. Science 350 (6258), 310–313 (1979).
Olive, J.A., Malatesta, L.C., Behn, M.D., Buck, W.R., 2022. Sensitivity of rift tectonics to global variability in the efficiency of river erosion. Proc. Natl. Acad. Sci. 119 (13) e2115077119.
Olive, J.A., Ekström, G., Buck, W.R., Liu, Z., Escartín, J., Bickert, M., 2024. Mid-ocean ridge unfaulting revealed by magmatic intrusions. Nature 1–6.
Paulatto, M., Canales, J.P., Dunn, R.A., Sohn, R.A., 2015. Heterogeneous and asymmetric crustal accretion: new constraints from multibeam bathymetry and potential field data from the Rainbow area of the Mid-Atlantic Ridge (36°15'N). Geochem. Geophys. Geosyst. 16 (9), 2994–3014. https://doi.org/10.1002/2015GC005743.
Rodríguez, C.E., Bommer, J.J., Chandler, R.J., 1999. Earthquake-induced landslides: 1980-1997. Soil Dyn. Earthq. Eng. 18 (5), 325–346. https://doi.org/10.1016/S0267-7261(99)00012-3.
Roering, J.J., Kirchner, J.W., Dietrich, W.E., 1999. Evidence for nonlinear, diffusive sediment transport on hillslopes and implications for landscape morphology. Water Resour. Res. 35 (3), 853–870. https://doi.org/10.1029/1998WR900090.
Roth, S., Granot, R., Downey, N.J., 2019. Discrete characterization of abyssal hills: unraveling temporal variations in crustal accretion processes at the 10°30′N segment, East Pacific Rise. Earth Planet. Sci Lett. 525, 115762. https://doi.org/10.1016/j.epsl.2019.115762.
Ryan, W.B.F., et al., 2009. Global multi-resolution topography synthesis. Geochem. Geophys. Geosyst. 10, Q03014. https://doi.org/10.1029/2008GC002332.
Searle, R.C., Laughton, A.S., 1977. Sonar studies of the Mid-Atlantic Ridge and Kurchatov Fracture Zone. J. Geophys. Res. 82, 5313–5328.
Searle, R.C., Cowie, P.A., Mitchell, N.C., Allerton, S., MacLeod, C.J., Escartin, J., et al., 1998. Fault structure and detailed evolution of a slow spreading ridge segment: the Mid-Atlantic Ridge at 29°N. Earth Planet. Sci. Lett. 154 (1–4), 167–183. https://doi.org/10.1016/s0012-821x(97)00160-x.
Seton, M., Müller, R.D., Zahirovic, S., Williams, S., Wright, N.M., Cannon, J., et al., 2020. A global data set of present-day oceanic crustal age and seafloor spreading parameters. Geochem. Geophys. Geosyst. 21. https://doi.org/10.1029/2020GC009214 e2020GC009214.
Smith, D.K., Escartin, J., Cannat, M., Tolstoy, M., Fox, C.G., Bohnenstiehl, D.R., Bazin, S., 2003. Spatial and temporal distribution of seismicity along the northern Mid-Atlantic Ridge (15°-35°N). J. Geophys. Res. Solid Earth 108 (B3). https://doi.org/10.1029/2002jb001964.
Smith, D.K., Schouten, H., Dick, H.J.B., Cann, J.R., Salters, V., Marschall, H.R., et al., 2014. Development and evolution of detachment faulting along 50 km of the Mid-Atlantic Ridge near 16.5N. Geochem. Geophys. Geosyst. 15 (12), 4692–4711. https://doi.org/10.1002/2014GC005563.
Smith, D.J., Naden, J., Miles, A.J., Bennett, H., Bicknell, S.H., 2018. Mass wasting events and their impact on the formation and preservation of submarine ore deposits. Ore Geol. Rev. 97, 143–151.
Stefanoudis, P.V., Schiebel, R., Mallet, R., Durden, J.M., Bett, B.J., Gooday, A.J., 2016. Agglutination of benthic foraminifera in relation to mesoscale bathymetric features in the abyssal NE Atlantic (Porcupine Abyssal Plain). Mar. Micropaleontol. 123, 15–28. https://doi.org/10.1016/j.marmicro.2015.12.005.
Thatcher, W., Hill, D.P., 1995. A simple model for the fault-generated morphology of slow-spreading mid-oceanic ridges. J. Geophys. Res. 100 (B1), 561–570. https://doi.org/10.1029/94JB02593.
Tominaga, M., Lyle, M., Mitchell, N.C., 2011. Seismic interpretation of pelagic sedimentation regimes in the 18-53 Ma eastern equatorial Pacific: basin-scale sedimentation and infilling of abyssal valleys. Geochem. Geophys. Geosyst. 12 (3). https://doi.org/10.1029/2010GC003347.
Tsang-Hin-Sun, E., Royer, J.Y., Perrot, J., 2016. Seismicity and active accretion processes at the ultraslow-spreading Southwest and intermediate-spreading Southeast Indian ridges from hydroacoustic data. Geophys. J. Int. 206 (2), 1232–1245.
Tucholke, B.E., Stewart, K.W., Kleinrock, M.C., 1997. Long-term denudation of ocean crust in the central North Atlantic Ocean. Geology 25 (2), 171–174. https://doi.org/10.1130/0091-7613(1997)025≤0171:LTDOOC≥2.3.CO;2.
Tucholke, B.E., Parnell-Turner, R., Smith, D.K., 2023. The global spectrum of seafloor morphology on mid-ocean ridge flanks related to magma supply. J. Geophys. Res. Solid Earth 128. https://doi.org/10.1029/2023JB027367 e2023JB027367.
Tucker, G.E., McCoy, S.W., Hobley, D.E., 2018. A lattice grain model of hillslope evolution. Earth Surf. Dyn. 6 (3), 563–582.
U.S. Geological Survey (2017). Earthquake hazards program, advanced national seismic system (ANSS) comprehensive catalog of earthquake events and products: various, available at https://earthquake.usgs.gov/data/comcat/ (last accessed October 2023).
Weaver, J., Eggertsson, G.H., Utley, J.E., Wallace, P.A., Lamur, A., Kendrick, J.E., Tuffen, H., Markússon, S.H., Lavallée, Y., 2020. Thermal liability of hyaloclastite in the Krafla geothermal reservoir, Iceland: the impact of phyllosilicates on permeability and rock strength. Geofluids 2020 (1), 9057193.
Webb, H.F., Jordan, T.H., 1993. Quantifying the distribution and transport of pelagic sediments on young abyssal hills. Geophys. Res. Lett. 20 (20), 2203–2206. https://doi.org/10.1029/93GL01881.
Webb, H.F., Jordan, T.H., 2001. Pelagic sedimentation on rough seafloor topography 2. Inversion results from the North Atlantic Acoustic Reverberation Corridor. J. Geophys. Res. Solid Earth 106 (B12), 30451–30473. https://doi.org/10.1029/2000jb900274.
Weissel, J.K., Karner, G.D., 1989. Flexural uplift of rift flanks due to mechanical unloading of the lithosphere during extension. J. Geophys. Res. 94 (B10). https://doi.org/10.1029/jb094ib10p13919.
Wolf, S.G., Huismans, R.S., Braun, J., Yuan, X., 2022. Topography of mountain belts controlled by rheology and surface processes. Nature 606 (7914), 516–521.
Wright, D.J., Haymon, R.M., Fornari, D.J., 1995. Crustal fissuring and its relationship to magmatic and hydrothermal processes on the East Pacific Rise crest (9° 12′ to 54′ N). J. Geophys. Res. Solid Earth 100 (B4), 6097–6120.